1   **Oxidation and Fume Formation from Liquid Silicomanganese Alloys Exposed to Atmospheres**

2   **Containing Moisture**

3   Yan Ma[1,3], Elmira Moosavi-Khoonsari[2], Håkon A Hartvedt Olsen Myklebust[3], Gabriella

4   Tranell[3]

5

6   [1]Department of Energy and Process Engineering, Norwegian University of Science and

7   Technology (NTNU), 7491 Trondheim, Norway

8

9   [2]Department of Mechanical Engineering, École de Technologie Supérieure (ÉTS), Montreal,

10   Quebec H3C 1K3, Canada

11

12   [3]Department of Materials Science and Engineering, Norwegian University of Science and

13   Technology (NTNU), 7491 Trondheim, Norway

14

15   Corresponding author: Elmira Moosavi-Khoonsari

16   Tel: +1(514)396-8800 (ext. 8702)

17   E-mail: elmira.moosavi@etsmtl.ca

18

28   **Abstract**

29   In industrial applications and laboratory studies, it has been shown that the use of water spray

30   may significantly reduce the amount of fume generated from the oxidation process of liquid

31   high carbon ferromanganese alloy. However, in our recent study, it was shown that the

32   oxidation rate of liquid silicon alloy increases with increasing water content in the

33   atmosphere. Therefore, in this paper, the effect of moisture on the oxidation and fume

34   formation of a liquid silicomanganese alloy was investigated. The fuming rate, fume

35   characteristics, and experimental observations from wet air experiments on the

36   silicomanganese melt were compared with those obtained from dry air experiments, and with

37   the results of wet air experiments conducted on high carbon ferromanganese and silicon melts.

38   In addition, the oxidation process of the silicomanganese and high carbon ferromanganese

39   melts was modeled under the experimental conditions, using FactSage 8.1 thermochemical

40   software, to better understand the equilibrium thermodynamic principles of the experimental

41   results. In general, there was good agreement between the simulated and experimentally

42   observed oxidation behavior of silicomanganese and high carbon ferromanganese melts under

43   moist air conditions.

44   **Keywords:** Silicomanganese, Ferromanganese, Wet air experiments, Oxidation, Fuming,

45   Thermochemical simulation

46

47
48
49
50
51

1. Introduction

In a manganese ferroalloy production plant, fugitive emissions are generated during most operations, *e.g.* materials handling and transportation, tapping, refining, and casting.[1] While mechanically generated particulate matters (PMs) are essentially, concerning composition, fine fractions of raw materials or products, the thermally generated fumes contain mainly metallic oxides formed from complex oxidation reactions between molten metal or metal vapor and oxygen in the atmosphere.[2] It should be noted that these PM emissions are considered among the major occupational health and safety challenges in the plant.

A limited number of industrial and laboratory studies have been carried out to investigate the fume formation mechanisms, involved in the thermal oxidation of manganese alloys.[3-8] To understand fuming mechanisms from both thermodynamic and kinetic points of view, the current authors[4-8] conducted laboratory-scale experiments by heating commercial ferroalloys in a closed graphite crucible, varying the gas composition and metal temperature, collecting the generated fume through a fume/gas extraction system, and analyzing the dust particles. In industrial applications, the installation of fine water sprays along the roof edges by the casting beds of ferromanganese (FeMn) alloys at Eramet Sauda, Norway, has resulted in a significant reduction of visible fume emissions.[9] This behavior was confirmed in a recent laboratory study,[10] but the phenomenon was only partly explained. The question, then, arouse whether the same type of water spray system would be equally effective for other types of ferroalloys such as ferrosilicon (FeSi)/silicon (Si) and silicomanganese (SiMn). However, as outlined in our recent study,[11] the same addition of water vapor to the atmosphere has the opposite effect on the fuming of liquid metallurgical grade silicon (MG-Si). As such, it is of both academic and industrial interest to understand the effect of moisture in the atmosphere on the fuming of SiMn alloy, which is the objective of the current study.

2. Theoretical Background

A standard SiMn alloy is composed of approximately 17 wt.% Si, 67 wt.% Mn, 9 wt.% Fe, 2 wt.% C and other trace elements (*e.g.* Mg, Ca, Na, etc.).[12] The oxidation of SiMn alloy in dry air was described by the current authors in a previous publication.[6] Manganese exhibits a high vapor pressure at elevated temperatures, and Si forms SiO gas at low oxygen partial pressures. Both gaseous species oxidize in air and produce complex fumes. In the melt temperature range 1673 K - 1773 K, the partial pressure of SiO is low and Mn is the main fume-forming gaseous species, resulting in predominantly crystalline manganese oxide in the fume. However, at higher melt temperatures, from 1773 K to 1873 K, the SiO partial pressure increases and most of the formed MnO reacts with SiO molecules/clusters, resulting in complex, amorphous $SiMnO_x$ particles. At melt temperatures higher than 1873 K, Mn evaporation is extensive, leading to a combination of the complex, amorphous $SiMnO_x$ and crystalline MnO_x particles.[6]

In addition, the formation of manganese hydroxide and oxyhydroxide gaseous species has been investigated.[13, 14] Hildenbrand et al.[13] studied the reactive vaporization of MnO under the presence of O_2 and H_2O/D_2O by effusion-beam mass spectrometry. With a mixture of O_2 and H_2O vapors injected into the system containing MnO at about 1900 K, the ions OH^+, $MnOH^+$, $Mn(OH)_2^+$, and $MnO(OH)^+$ were observed. As Mn has multiple oxidation states, these authors commented that $Mn(OH)_3(g)$ and $MnO(OH)_2(g)$ could also form at high pressures. Opila[14] reported that Mn oxyhydroxide gaseous species must also exist, but additional work is needed to identify the unknown Mn-O-H(g) species and to determine corresponding thermodynamic data. This will enable the prediction of oxide stability under water vapor at high temperatures. Currently, the thermodynamic data available in the

99 FactSage SGPS thermochemical database for the Mn-O-H vapor species include Mn(g),

100 $MnO(g)$, $MnO_2(g)$, $MnH(g)$, and $MnOH(g)$.[14, 15]

101 In the exposure of SiMn ferroalloys to water vapor, there are several possible reactions

102 between the water vapor/oxygen and Mn vapor/liquid Mn, resulting in MnO/MnOH

103 formation. These reactions are listed below together with the associated Gibbs energies of the

104 reactions, calculated from 273 K to 2273 K using FactSage 8.1 FactPS and FToxid databases

105 (the Gibbs energy of formation of MnOH species was taken from the FactSage SGPS

106 database).[16] These reactions are expected to take place, concurrently, with the oxidation of

107 Si species, previously shown:[10]

$Mn(l)=Mn(g)$ $\Delta G^o(kJ)= 256.484-0.112T(K)$ (1)

Active oxidation:

$Mn(g)+H_2O(v)=MnO(l/s)+H_2(g)$ $\Delta G_l^o(kJ)= -356.043+0.116T(K)$ (2)

$\Delta G_s^o(kJ)= -410.435+0.142T(K)$

$Mn(g)+1/2O_2(g)=MnO(l/s)$ $\Delta G_l^o(kJ)= -603.302+0.172T(K)$ (3)

$\Delta G_s^o(kJ)= -657.693+0.197T(K)$

$Mn(g)+OH(g)=MnOH(g)$ $\Delta G^o(kJ)= -304.126+0.106T(K)$ (4)

$Mn(g)+1/2O_2+1/2H_2=MnOH(g)$ $\Delta G^o(kJ)= -265.944+0.092T(K)$ (5)

$Mn(l)+OH(g)=MnOH(g)$ $\Delta G^o(kJ)= -47.642-0.006T(K)$ (6)

$Mn(l)+1/2H_2(g)+1/2O_2(g)=MnOH(g)$ $\Delta G^o(kJ)= -9.460-0.021T(K)$ (7)

Passive oxidation:

$Mn(l)+H_2O(v)=MnO(l/s)+H_2(g)$ $\Delta G_l^o(kJ)= -99.559+0.004T(K)$ (8)

$\Delta G_s^o(kJ)= -153.951+0.029T(K)$

$Mn(l)+1/2O_2(g)=MnO(l/s)$ $\Delta G_l^o(kJ)= -346.817+0.059T(K)$ (9)

$\Delta G_s^o(kJ)= -401.209+0.085T(K)$

108 As seen from equations (2)-(9), all the reactions are expected to occur at high temperatures,

109 and they are all exothermic reactions.

110 **3. Experimental and modeling work**

111 *3.1 Experimental work*

112 The effect of introducing moisture in the dry synthetic air on the oxidation rate and products

113 of SiMn melt was experimentally investigated in the same set-up as described, previously, by

114 the current authors.[11] A standard grade SiMn alloy was used for the investigation (see

115 above). As the composition and morphology of SiMn fume in dry air vary with melt

116 temperature,[6] experiments were carried out at two temperatures 1723 K and 1873 K under

117 different water vapor pressures. In addition, in this work, the oxidation behavior of high

118 carbon ferromanganese (HCFeMn) alloy was investigated at 1823 K under different water

119 vapor pressures to corroborate the previous laboratory results, where the oxidation behavior

120 of the HCFeMn melt was studied at 1773 K.[10] It should be added that the inner and outer

121 diameters of the gas lance were 5 mm and 17 mm, respectively. The lance tip was placed

122 about 20 mm above the liquid melt during each experiment. The experimental matrix is given

123 in Table I. Since a graphite crucible was used for the experiments, the bulk alloys were

124 saturated with carbon. As such, the gas in contact with the liquid metal is assumed to have an

125 equilibrium pressure of CO(g). As discussed by Myklebust et al.,[8] the surface of a bulk C-

126 saturated FeMn alloy may be depleted in C, giving it a different Mn (and Si) activity than the

127 bulk and as such, affecting the effective vapor pressure of alloy species. Water vapor pressure

128 at a given temperature was calculated from the Antoine equation:[17]

129

$$\ln P_v \text{ (Pa)} = 23.1963 - \frac{3816.44}{T(K) - 46.13} \tag{10}$$

130   where P_v and T denote water vapor pressure and the absolute temperature, respectively. The

131   water vapor pressures calculated from Eq. (10) lie within 0.1 percent of values from steam

132   tables over the temperature range 323-373 K. At the temperatures 298 and 313 K, errors less

133   than 3% are expected.

134   Table I. Experimental matrix of the current work

Alloy	Gas	Melt temp (K)	Water vapor pressure (kPa)	No. of parallels	Holding time (min)
	Synthetic air	1723	7.36	1	25
	Synthetic air	1723	12.33	1	40
	Synthetic air	1723	19.92	1	40
	Synthetic air	1723	25.01	1	40
Standard SiMn	Synthetic air	1873	0	1	30
	Synthetic air	1873	3.14	3	30, 30, and 40[1]
	Synthetic air	1873	7.36	3	30, 30, and 40[2]
	Synthetic air	1873	12.33	4	20, 30, and 40
	Synthetic air	1873	19.92	3	20, 30, and 40
HC FeMn	Synthetic air	1823	0	4	20
	Synthetic air	1823	7.36	3	20
	Synthetic air	1823	12.33	4	20

   1) & 2) These experiments were repeated two times for the holding time of 30 min.

135

136   Each experiment was performed using 4 kg standard SiMn alloy or HCFeMn alloy. During

137   the experiments, dry synthetic air was initially passed through the humidifier at the rate of 3

138   L/min to achieve the desired humidity, before being blown above the metal surface. After the

139   experiments, the fume was collected at three sites: the so-called transition tube, the cooler,

140   and the filter. The majority of fume was collected from the filter. To avoid free water,

141   remaining in the fume, the collected fumes together with the transition tube, cooler, and filter

142   fabric were directly weighed after the experiments and reweighed after being dried for at least

143   20 min at 383 K to compare the differences.

144   The total amount of fume generated in each experiment was measured, and the mass flux, J_m,

145   was calculated as follows:

$$J_m = \frac{m}{At} \tag{11}$$

146   where m is the total mass of fume generated (using the data obtained after dryer), A is the

147   surface area of the molten metal (assuming no surface oxide/slag coverage), and t is the

148   holding time of the experiment.

149   Fume samples from some of the experiments were characterized using scanning electron

150   microscopy (SEM), transmission electron microscopy (TEM), and inductively coupled

151   plasma mass spectrometry (ICP-MS). The equipment used for SEM was a Zeiss Supra 55 PV

152   field emission microscope. Only the fume samples, collected from SiMn melt at 1723 K,

153   were enough for SEM observations. Particle size distributions were estimated with the aid of

154   both laser diffraction (LD), assuming an average density model, and visual SEM image

155   counting. The composition of slag formed on the alloy surface as a result of the surface

156   oxidation/passivation process was determined using electron probe micro-analysis (EPMA).

157   *3.2 Equilibrium thermodynamic modeling*

158   Similar to the liquid Si system, the thermochemical simulation of the SiMn oxidation

159   experiments were performed at 1723 K and 1873 K, and thermochemical modeling of

160   HCFeMn oxidation experiments was also conducted at 1773 K and 1823 K, using FactSage

161   8.1 thermochemical package[16] to explain the experimental results from the equilibrium point

162   of view. No kinetic factors were taken into account in the model. Thermodynamic properties

163   of the SiMn and HCFeMn melts were taken from the FactSage FTlite database while those of

164   oxides were adopted from the FToxid database. Gibbs energies of gaseous species were taken

165   from the FactPS database except for $SiO(OH)_2$, $Si(OH)_4$, and MnOH, adopted from the SGPS

166   database.

167   The oxidation of the melt and its fuming process were simulated as three effective

168   equilibrium reaction zones, shown in Figure 1: (R1) the reaction between the liquid metal

169   surface and gas jet, which generates a gas phase here called "fume 1"; (R2) the reaction

170   between "fume 1" and surrounding gas phase across the interface, leading to the formation of

171   "fume 2" with an altered composition in comparison to "fume 1"; and (R3) the fume

172   condensation while exiting the reaction zone 2 due to cooling of the system. More details

173   about the thermodynamic modeling approach and flow of the reactions have been provided in

174   the previous work.[11]
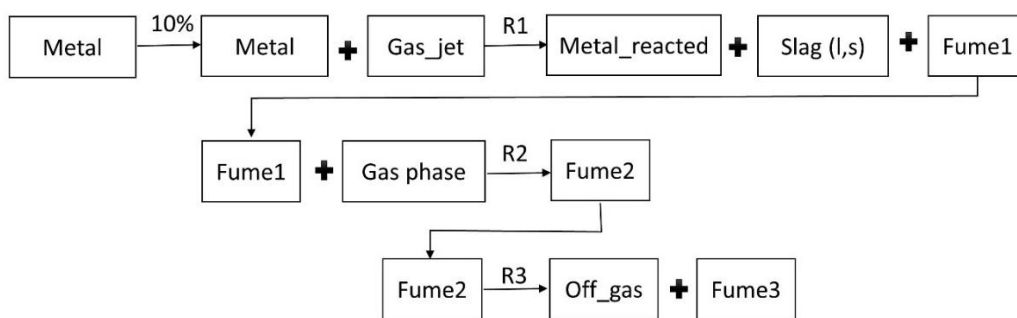
175

176   Fig. 1 – Flow of equilibrium calculations for simulation of fuming from oxidation process of

177   the melt. Reprinted with permission from reference [11]. Copyright *2019* American Chemical

178   Society.

4. Results and discussion

4.1 General observations from SiMn experiments

Visible turbid droplets were found on the filter fabric from the SiMn experiments at 1723 K only when water vapor pressure was above 12 kPa. However, no visible droplets were found in 1873 K SiMn experiments, and there was almost no mass difference before and after drying the fume-containing parts of the equipment.

Blisters were visually observed on the cooled metal surface after the experiments at 1723 K in wet air. The blisters seemed to increase with an increasing water vapor pressure at 1723 K experiments. No blisters were found in the dry air experiments.

The formation of a slag layer on the cooled metal surface was also visible after the SiMn experiments at 1873 K. The slag layer was removed from the metal surface for further characterization. As presented in Figure 2, the slag exhibits two different types of morphology and composition. The compositions of slag in zones 1 and 2 are given in Table II. The main slag phase (marked 1) is mainly composed of SiO_2 and MnO, as well as other minor/trace species. Silica crystals, precipitated during cooling, are marked as zone 2. The slag formation on the metal surface suggests that the surface exposed to air/oxygen (from which fume can form) might be dynamic, making an accurate determination of fume flux challenging.
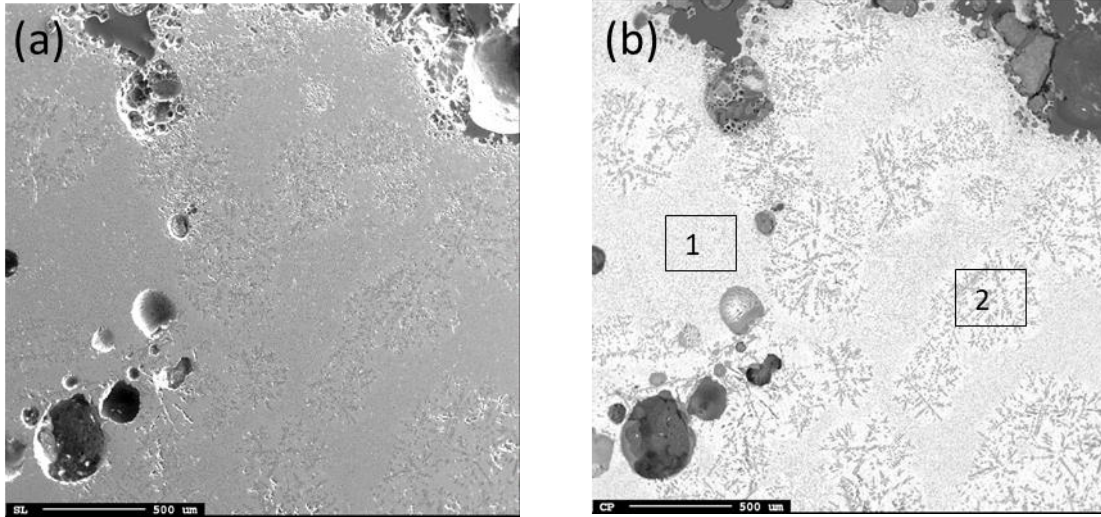
10

Fig. 2 – Electron images of slag obtained from SiMn wet air experiments at 1873 K; (a) secondary electron (SE), and (b) backscattered electron (BSE) modes.

Table II. Slag composition measured using EPMA (wt.%)

Zone	SiO_2	Na_2O	K_2O	MnO	MgO	CaO	FeO	Al_2O_3	P_2O_5	ZnO	SO_3	TiO_2	Total
1	54.82	0.16	0.16	27.60	2.01	4.86	0.08	4.89	0.02	0.00	0.55	0.50	95.64
2	96.35	0.07	0.00	0.96	0.02	0.13	0.00	0.34	0.02	0.06	0.00	0.00	97.95

4.2 Measured mass flux

The mass fluxes of fumes obtained from the oxidation process of SiMn alloy at the two temperatures of 1723 K and 1873 K under different water vapor pressures are depicted in Figure 3 and compared to results from the FeMn experiments at 1773 K from the earlier work,[10] and 1823 K from this work. The dry synthetic air experiments are presented at water vapor pressure equal to 0 kPa. As seen in Figure 3, the mass fluxes of fumes from the FeMn melt at both 1773 K and 1823 K decrease with increasing water vapor pressure. For the SiMn melt, although the mass flux largely fluctuates, it shows a relatively constant trend for both temperatures and different water vapor pressures.
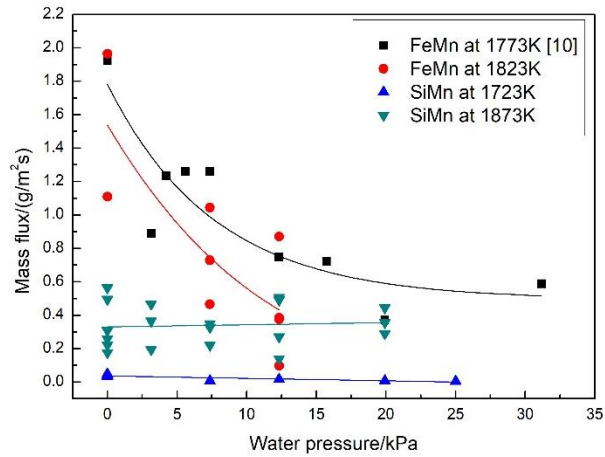
11

210

Fig. 3 – Mass fluxes of fumes from the FeMn and SiMn melts under different water vapor

pressures.

The variations between results of the repeated SiMn experiments under the same water vapor

pressure may be explained, at least partly, by the observations of slag formation on the metal

surface. The slag formation leads to partial passivation as the alloy surface, exposed to

oxygen (where the fume formation and active oxidation take place), becomes non-static.

A comparison between the average mass flux from the SiMn melt at 1873 K and the Si melt

at 1823 K is shown in Figure 4. The mass flux from the Si melt increases with increasing

water content in the gas jet up to 7.4 kPa, as illustrated in our previous paper.[11, 18] With a

further increase in water vapor pressure, the mass flux from Si melt levels off at

approximately the same level as that from the SiMn alloy.
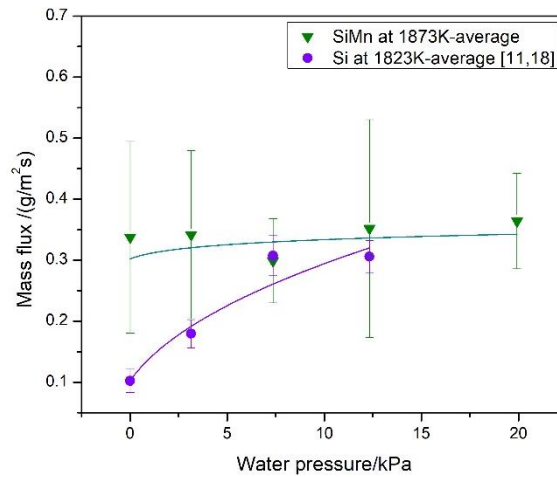
222

Fig. 4 – Average mass flux of fume from Si melt at 1823 K and SiMn melt at 1873 K as a function of water vapor pressure.

4.3 Fume morphology

Scanning electron micrographs of typical fume particles obtained from the SiMn alloy melt at 1723 K and 1873 K, in dry and wet air, are shown in Figure 5.

As presented in Figures 5a and b, the fume particles, which formed from the oxidation of SiMn melt at 1723 K in dry and wet air conditions, respectively, have very different morphologies. Particles formed in moist air are coarser and more agglomerated, suggesting that the fume formation mechanism is altered by the introduction of water vapor.

The morphologies of fume particles formed from the oxidation of SiMn melt under dry and wet air conditions at 1873 K are depicted in Figures 5c and d, respectively. The SEM images indicate that, while fume particles are spherical in both wet and dry conditions, particle aggregation is more pronounced under humid conditions.
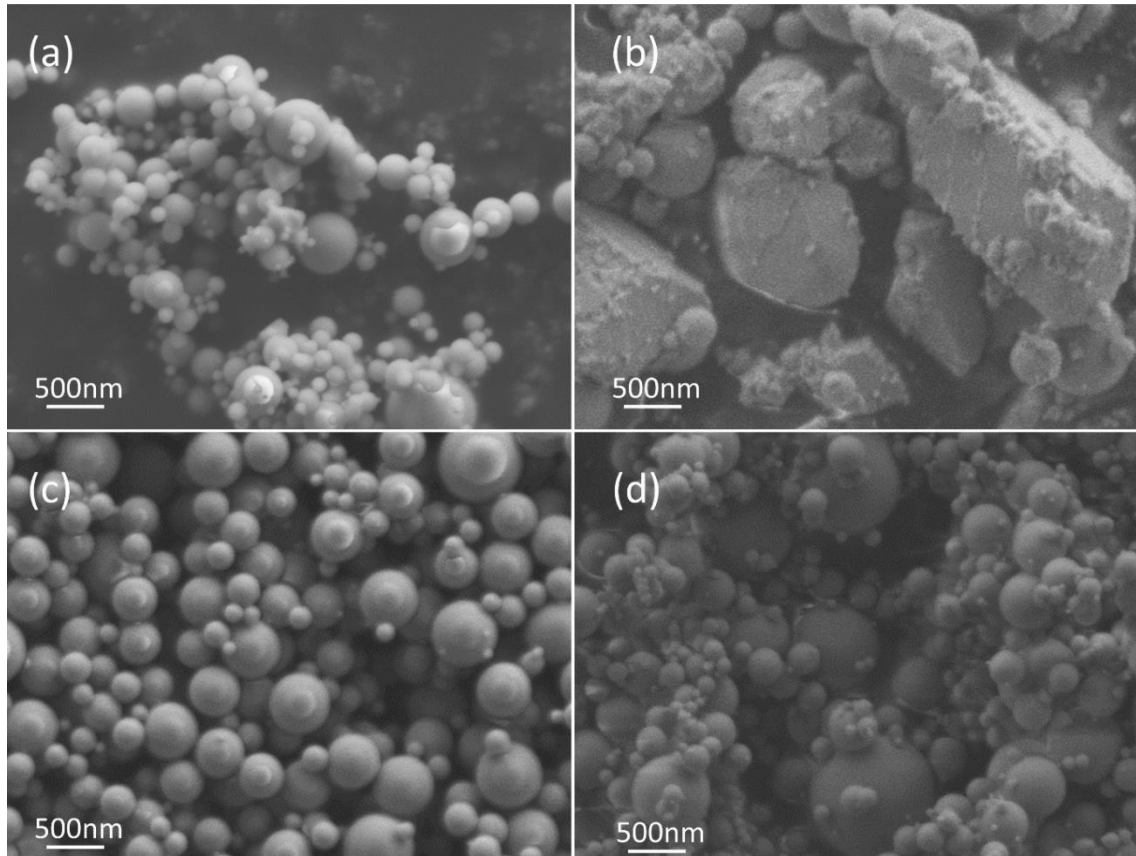
Fig. 5 – Typical morphology of SiMn filter fume, generated at (a) 1723 K dry air, (b) 1723 K wet air, (c) 1873 K dry air, and (d) 1873 K wet air conditions.

The fume samples from the transition tube, obtained from the oxidation of SiMn melt at 1873 K under wet air conditions, were also investigated using TEM, shown in Figure 6. The TEM bright-field image of the transition tube fume, which formed from SiMn alloy under wet air conditions, is illustrated in Figure 6a. A fraction of particles with uneven surfaces are crystalline, and others with smooth surfaces are amorphous. Electron energy loss spectroscopy (EELS) mapping was carried out to determine the distribution of Si and Mn in these particles, and the results are depicted in Figure 6b. The edges of all the crystalline particles are covered by Mn (marked green), while the cores of the crystalline particles consist of a combination of Si and Mn. The amorphous particles are composed of both Si and Mn with no compositional differences around the edges.
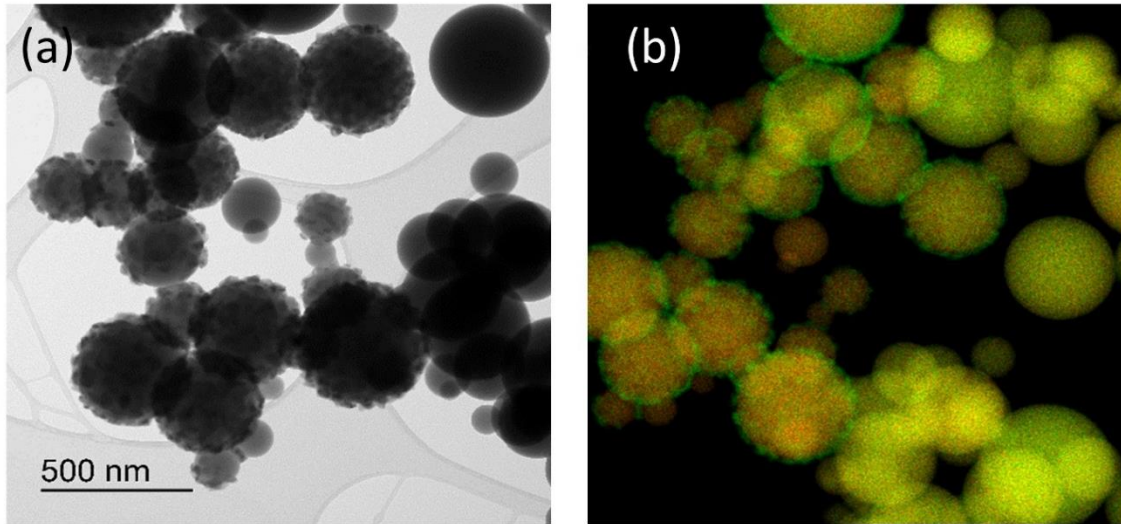
14

500 nm

Fig. 6 – Transition tube fume from SiMn experiments at 1873 K under wet air conditions; (a) TEM bright-field image, (b) relative concentrations of Mn (green color) and Si (red color) in the EEL spectrum image.

Figure 7 illustrates the TEM image of SiMn filter fume at 1873 K under wet air conditions. As seen, the particles are all spheres of various sizes and are all amorphous. The elements are found to be evenly distributed over the entire mapping area. This was also observed in our previous studies on dry air SiMn oxidation.[6] The TEM results indicate that there are no compositional differences in the fume particles obtained under both dry and wet air conditions.

1 µm
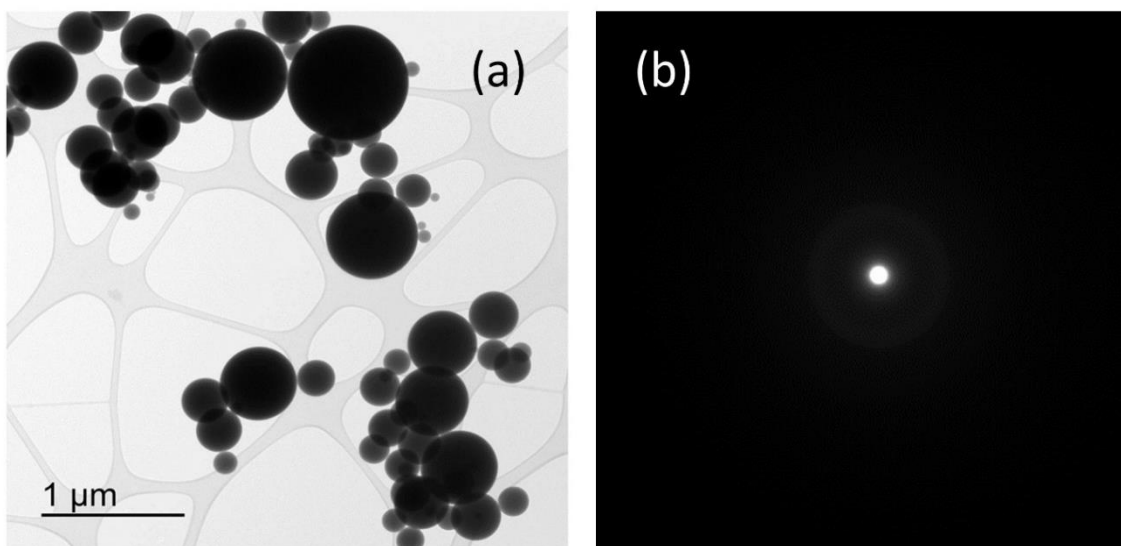
260   Fig. 7 – Filter fume from SiMn experiments at 1873K under wet air conditions; (a) TEM

261   bright-field image, and (b) selected area electron diffraction pattern.

262   *4.4 Main elements in SiMn fume at 1873 K*

263   As outlined above, there is no major morphological difference in the protoparticles[1] of SiMn

264   fume at 1873 K between dry and wet air conditions, and TEM analysis indicates no

265   compositional differences. ICP-MS analysis of the fume was carried out to further reliably

266   compare the concentrations of the main elements (Si and Mn) in the SiMn fume. The

267   concentrations of Si and Mn in the fume are shown in Figure 8 under different water vapor

268   pressures. The experimental error range for Si and Mn concentrations in the fume is ±5 wt%.

269   ICP-MS analysis supports the TEM observation. That is, there is no significant difference in

270   the concentrations of main elements in the fume with increasing water vapor pressure.
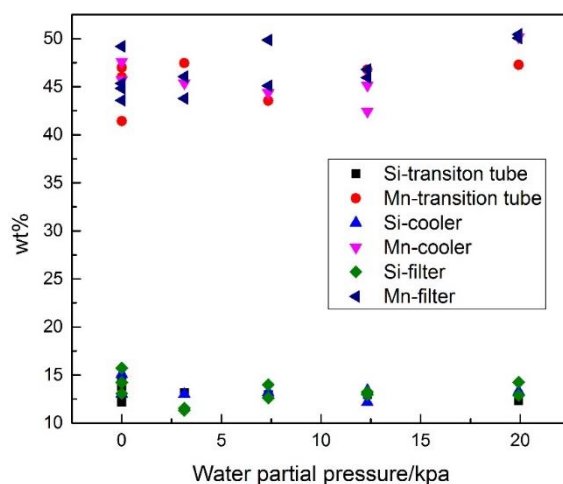
271

272   Fig. 8 – Concentrations of Si and Mn in the SiMn fume at 1873 K as a function of water

273   vapor pressure.

274

275   *4.5 Particle size distribution*

---

[1] Protoparticles are, here, defined as the smallest visible particle unit.

276   The particle size distribution of SiMn filter fume was analyzed using both LD and SEM

277   image

278   analysis. The LD distribution indicates the size of agglomerates[2] in the fume samples, while

279   the SEM image counting represents the size of protoparticles.

280   The particle size distributions of SiMn fume which formed at 1873 K under both dry and wet

281   air conditions are shown in Figure 9. As seen, the particle size distribution appears to have

282   very similar shapes under different water vapor pressures. It seems that the injection of water

283   does not have a significant effect on the protoparticle size or the agglomerated particle size.

284
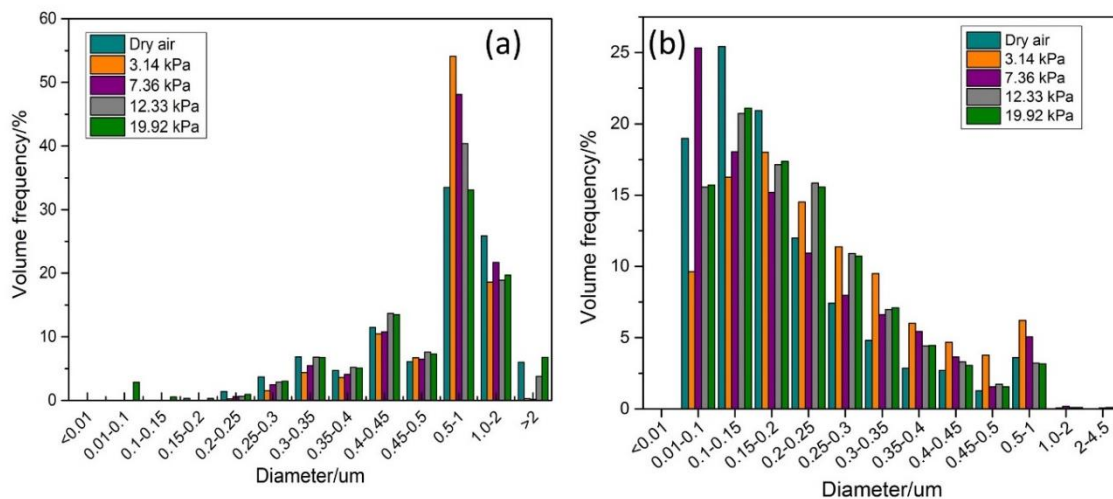
285

286   Fig. 9 – Particle size distribution of filter fume from SiMn melt at 1873 K under different

287   water vapor pressures, obtained using (a) LD and (b) SEM image counting.

---

[2] Agglomerates are clusters of proto-particles joined by bonds not dissolved by immersion of the particulate matter in the solution media used for laser diffraction analysis.

17

288   *4.6 Equilibrium thermodynamic modeling results*

289   The calculated reaction products from the oxidation process of the SiMn and HCFeMn melts

290   by the gas jet (synthetic air with water vapor) are illustrated in Figures 10 - 15. All of the

291   three reaction zones, depicted in Figure 1, are described below.

292

293   4.6.1. Oxidation of SiMn melt

294   **SiMn melt and gas jet reaction (R1)**

295   The reaction of SiMn melt and gas jet (R1) leads to the formation of SiO_2 slag and a gaseous

296   phase; here called 'fume 1' (see Figure 10a), which composition is shown in Figure 10b. The

297   left columns represent the calculations at 1873 K and the right columns represent the

298   calculations at 1723 K. Fractions of metal and gas phases reacting together could not be

299   measured during the experiments. However, it could be assumed that a small fraction of

300   metal reacted with the gas jet at the metal surface. Therefore, for R1, we tested the reactions

301   between different fractions of the melt (e.g. 10%, 20%, etc.) and the gas phase, and there

302   were no changes in the results. For the gas phase, the water vapor pressure in the air was

303   varied according to the experimental conditions to simulate the metal-gas reaction (R1).

304   Moreover, temperature measurement using a thermocouple revealed that the gas jet reached

305   the melt temperature when exiting the lance and at the time of reaction with the melt. This is

306   because the experimental gas flow rate was rather low (3 L/min). As a result, the same

307   temperature as that of bulk liquid metal was used for the gas jet in simulating R1.

         1873 K   1723 K
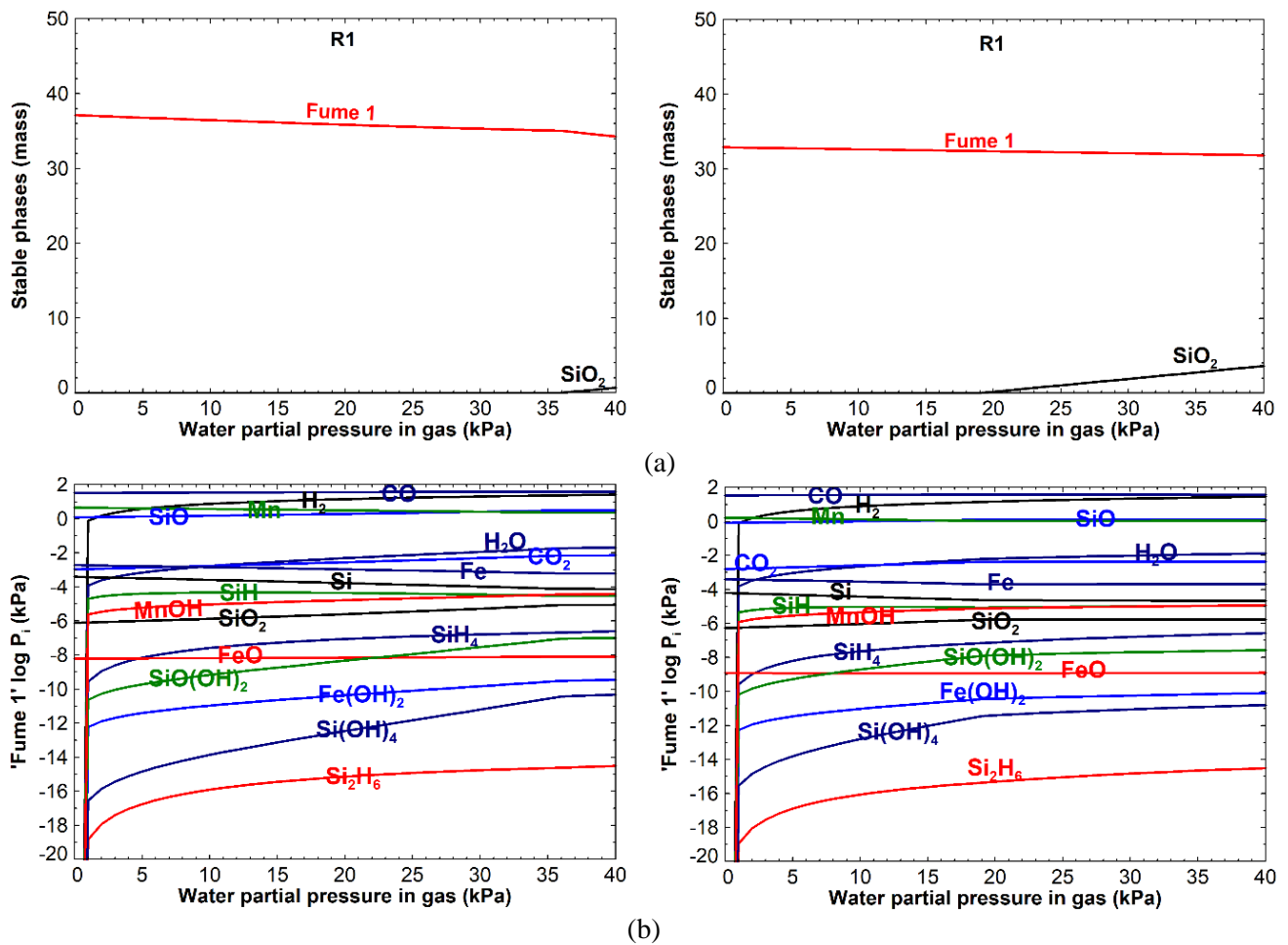
Fig. 10 – Simulated fuming from R1 under different water vapor pressures; (a) reaction products of the gas jet and SiMn melt, and (b) partial pressures of the gaseous species in 'fume 1'.

308   As seen in Figure 10a, the amount of generated fume decreases with increasing water partial

309   pressure in the gas phase. It is illustrated in Figure 10b that the partial pressures of gaseous

310   species decrease in the following order: Mn, SiO, Fe, Si, SiH, MnOH, SiO_2, SiH_4, $SiO(OH)_2$,

311   FeO, $Fe(OH)_2$, $Si(OH)_4$, and Si_2H_6. Partial pressures of Mn and Fe are much higher than that

312   of MnOH, and those of FeO and $Fe(OH)_2$, respectively, which is opposite to the case of Si

313   and SiO gaseous species. The Mn partial pressure slightly decreases and that of MnOH

314   increases by less than 1 order of magnitude. A similar behavior from Fe and $Fe(OH)_2$ is seen

315   (the partial pressure of $Fe(OH)_2$ increases by 2 to 3 orders of magnitude). However, Mn

316   vapor is dominant in comparison to MnOH (P_{Mn} is about 6 orders of magnitude larger than

317   P_{MnOH}); therefore, the Mn overall partial pressure slightly decreases. It is seen that the partial

318   pressures of SiO and SiO_2 slightly increase by less than 1 order of magnitude while the partial

319   pressures of Si hydrides and (oxy)hydroxides (SiH, SiH_4, Si_2H_6, $SiO(OH)_2$, and $Si(OH)_3$)

320   increase within 5-6 orders of magnitude within the calculated range of water vapor pressure

321   (*i.e.* up to 40 kPa).

322   In addition, as shown in Figure 10a, the amount of 'fume 1' calculated at 1873 K is higher

323   than that at 1723 K, and the 'fume 1' gaseous species at both temperatures show similar

324   trends. A small amount of SiO_2 slag also forms during the process at high temperatures on the

325   SiMn melt surface. However, according to observations (see figure 2), MnO-SiO_2 slag

326   formed on the metal surface. It should be noted that the melt surface could not be directly

327   observed at high temperatures during the experiments. Therefore, the difference in slag

328   composition from observations and calculations might be explained by cooling down the

329   crucible containing melt outside the furnace in ambient conditions after the experiments (*i.e.*,

330   Mn was also oxidized from the hot surface of the melt, exposed to the atmosphere, to form

331   MnO-SiO_2 slag).

332   **Oxidation reaction across the interface between melt surface and surrounding gas phase**

333   **(R2)**

334   The oxidation reaction of 'fume 1' at the interface between melt surface and surrounding gas

335   phase (R2) leads to the formation of liquid droplets dispersed in a gas phase, here called

336   'fume 2' (see Figure 11a). The compositions of liquid and gas components of 'fume 2' are

337   shown in Figures 11b and c, respectively. In Figure 11b, only the Mn- and Si-containing

338   vapor species are presented. The other dominant gaseous species are CO, N_2, CO_2, H_2O, O_2,

339   H_2, and OH.

           1873 K   1723 K
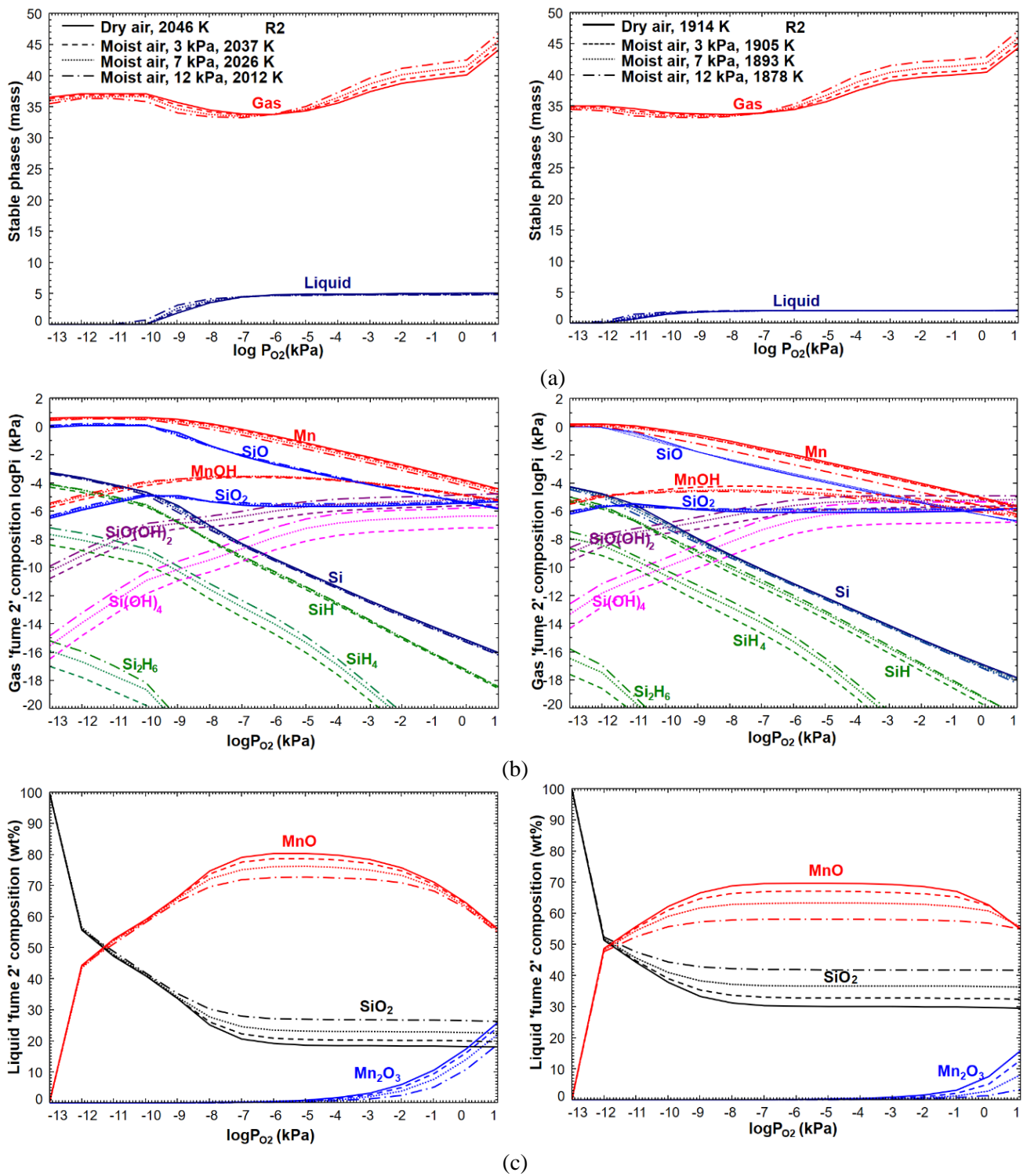
Fig. 11 – Simulated fuming from R2 under different water vapor pressures; (a) reaction products across the interface between SiMn melt surface and the surrounding gas, (b) composition of the gaseous 'fume 2', and (c) composition of liquid 'fume 2'. The labeled temperatures come from the adiabatic reaction in R1.

340

341 The labeled temperatures in figure 11a come from the adiabatic reaction in R1. During the

342 experiments, the bulk melt was continuously heated in an induction furnace. For example, for

343 SiMn experiments, the bulk liquid metal was heated to either 1873 K or 1723 K and kept at

344 those temperatures during the experiments. Therefore, it could be assumed that the adiabatic

345 reaction only locally raised the interfacial temperature. That is, the temperature increase is

346 only a local effect at the interface due to the adiabatic reaction. As a result, the interface

347 temperature including the temperatures of "fume 1", "fume 2", and surrounding gas adjacent

348 to the interface could be expected to be controlled by the adiabatic reaction (R1). Therefore,

349 we assumed the temperature gradient is negligible at the interface (*i.e*. R2 was calculated

350 isothermally).

351 The most important implication of the mixing ratio between the "fume 1" and surrounding

352 gas at the interface will be the change in the oxygen partial pressure. Therefore, for R2, we

353 considered changes in oxygen partial pressure across the interface. That is, the oxygen partial

354 pressure across the interface was set to vary from 10^{-13} kPa from the C saturated metal

355 interface at the left of the x-axis to an oxygen partial pressure of ~1 kPa, the bulk air partial

356 pressure on the far right of the x-axis. The individual lines were calculated at a constant

357 temperature imposed by the adiabatic reaction at the interface from R1. As shown in Figure

358 11a, the total amount of 'fume 2' is larger at 1873 K in comparison to that at 1723 K. The

359 amount of gaseous component of 'fume 2' does not change significantly from 1873 K to

360 1723 K but the mass of liquid component increases by 2 – 3 times. There is not a significant

361 difference in the amount of fume products (gas and liquid) with different moisture contents.

362 As depicted in Figure 11a, both liquid and gas phases of 'fume 2' show an overall increasing

363 trend with increasing oxygen partial pressure. The gaseous part of 'fume 2' is initially almost

364 constant, then decreases with increasing oxygen partial pressure from 10^{-10} and 10^{-12}, up to

365 about 10^{-6} and $10^{-7.5}$ kPa, at 1873 K and 1723 K, respectively, upon the formation of liquid

366 droplets of 'fume 2'. With further increasing the partial pressure of oxygen, the amount of

367 gaseous fume increases, and that of liquid fume stays constant.

368 As seen in Figure 11b, the partial pressures of SiO(g) and Mn(v) decrease with the formation

369 of the liquid fume at oxygen partial pressures of 10^{-10} and 10^{-12} kPa at 1873 K and 1723 K,

370 respectively. That is, the formation of condensed species (SiO_2 and MnO) is

371 thermodynamically more favorable. The partial pressures of Si and its hydrides, as well as

372 SiO, decrease due to oxidation reactions of Si species; and as a result, SiO_2 and

373 (oxy)hydroxides' partial pressures increase with increasing oxygen partial pressure. In

374 addition, it is clear that with increasing the water partial pressure in the gas phase, the

375 concentration of Si gaseous species increases while that of Mn gaseous species decreases. It

376 is also seen that the partial pressures of Si (oxy)hydroxide gaseous species increase with

377 decreasing temperature from 1873 K to 1723 K, which can be explained by a decrease in the

378 Gibbs energy of formation of (oxy)hydroxides species with decreasing temperature.

379 Figure 11c shows that the liquid component of 'fume 2' mainly consists of MnO, SiO_2, and

380 Mn_2O_3. With increasing oxygen partial pressure across the interface, the amount of MnO

381 drastically increases and the amount of SiO_2 sharply decreases up to around 10^{-7} kPa at 1873

382 K. At this point, MnO concentration reaches a maximum, SiO_2 content of liquid 'fume 2'

383 becomes constant, and Mn_2O_3 starts to form. The amount of Mn_2O_3 increases with further

384 increasing partial pressure of oxygen above 10^{-7} and 10^{-4} kPa at 1873 K and 1723 K,

385 respectively, while the formation of MnO decreases. Therefore, the liquid component of

386 'fume 2' changes in composition from a mixture of MnO and SiO_2 to a final mixture of MnO,

387 SiO_2 and Mn_2O_3. Moreover, the amounts of MnO and Mn_2O_3 species of the fume decrease

388 with increasing water vapor pressure while that of SiO_2 increases.

23

Fume condensation and off-gas formation (R3)

When the 'fume 2' exits the interface between the melt surface and surrounding gas, part of it condenses. This process is simulated as R3. The fume condensation leads to the formation of particles dispersed in a gas phase, here called 'fume 3'. The oxygen partial pressure at the interface in equilibrium with the carbon saturated metal could be calculated from the chemistry of the system. However, the oxygen partial pressure at the interface adjacent to the surrounding gas phase could not be determined with certainty and is expected to be lower than the bulk air oxygen potential. This can be justified by the occurrence of other reactions, which consume oxygen and form $CO(g)$, *e.g.* the reaction between oxygen in the surrounding and carbon from the graphite crucible. Therefore, for the calculation of R3, the oxygen partial pressure at the bulk gas interface was assumed to be about 10^{-1} kPa. Hence, the reaction products generated at oxygen partial pressure of 10^{-1} kPa were quenched using Scheil-Gulliver cooling mode, and the modeled fume components from R3 are shown in Figure 12. It is believed that Scheil cooling gives a good estimation of solute redistribution during the cooling of the gas phase. The uncondensable part of the fume exits the system as the off-gas (not shown in the figure), where N_2, CO_2, and H_2O are the main constituents. As illustrated in Figure 12a, the fume from the SiMn melt mainly contains an amorphous phase, which is the cooled liquid fume from R2. This result is in accordance with the experimental observation (see Figure 7). The main components of the amorphous fume are MnO (> 70 wt%), SiO_2 (15 – 20 wt%) and

1873 K   1723 K
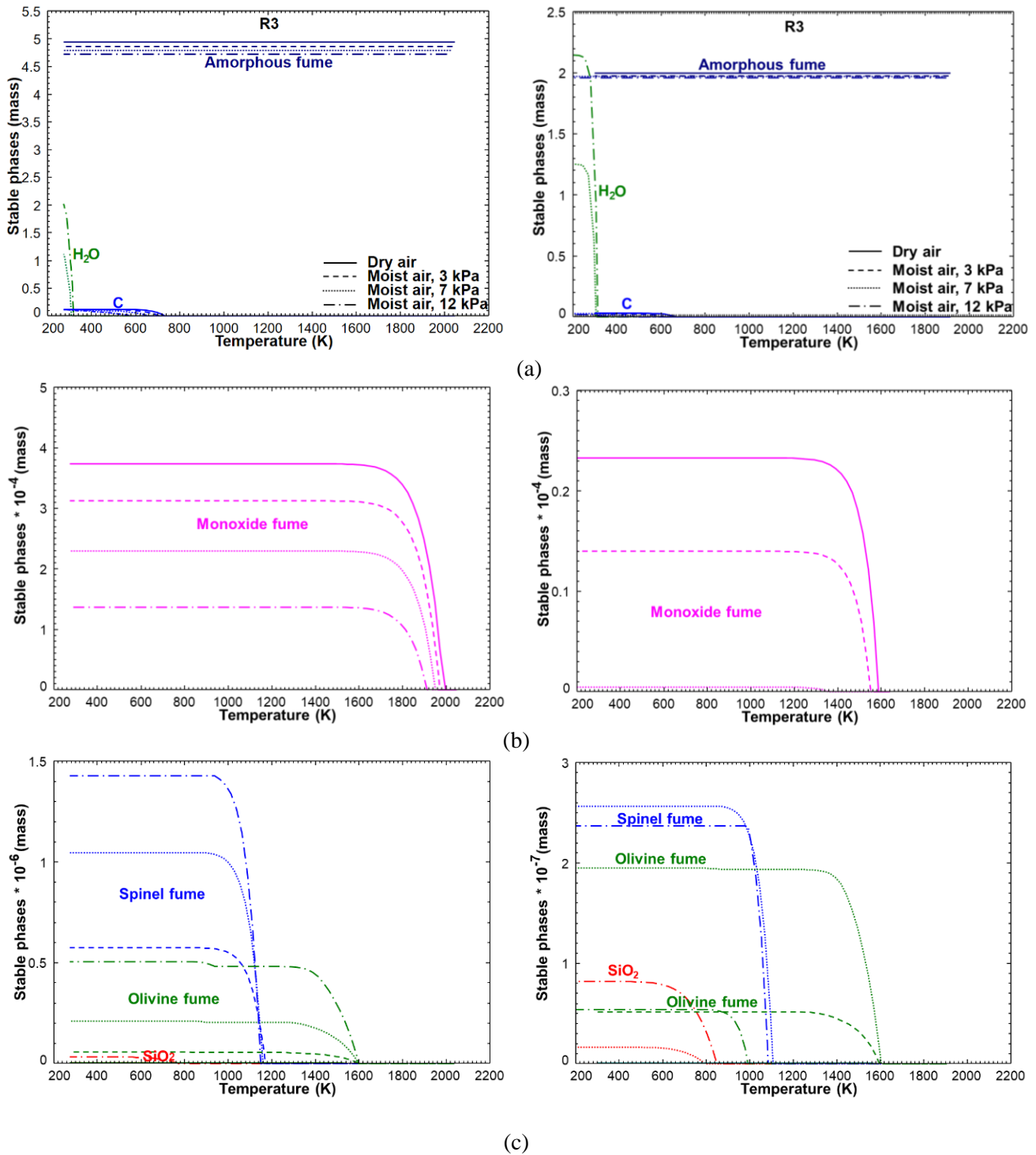
Fig. 12 – Simulated SiMn fuming from R3 under different water vapor pressures; (a – c) condensed fume components.

409

410   Mn_2O_3 (10 wt%). Carbon also precipitates out, perhaps in the form of soot, from the fume

411   below 773 K. Moreover, for water vapor pressures above 3 kPa, free water condenses around

412   333 K. This somehow agrees with the water droplets found on the filtered fume for water

413   vapor pressures above 12 kPa at 1723 K.

414   The condensed fume also contains minor crystalline phases such as monoxide, olivine, spinel,

415   and SiO_2, precipitating out of the gaseous component of 'fume 2' while cooling. The

416   monoxide phase is a solid solution, containing mainly MnO, and less than 1.0 wt% and 0.1 wt%

417   Mn_2O_3 and FeO_x, respectively. Olivine mostly contains Mn_2SiO_4, and the spinel's main

418   constituent is Fe_3O_4. However, the minor phases were not experimentally detected, probably

419   because (1) they occurred in extremely lower concentrations (at least by an order of 10^4) in

420   comparison to the amorphous fume, according to the calculations (see Figure 12), and (2) the

421   collected and analyzed fume from the experiments was inhomogeneous.

422   As revealed by the calculation of R3 and described above, the amount of fume stays almost

423   constant with increasing water vapor pressure and only very slightly decreases.

424   As presented in Figure 10b, the formation of Si fume can be explained by the formation of

425   SiO, SiO_2, SiH_4, $SiO(OH)_2$, $Si(OH)_4$, and Si_2H_6 gaseous species. While partial pressures of Si

426   hydrides and (oxy)hydroxides increase by a few orders of magnitude, the vapor pressure of

427   the dominant species SiO is almost constant and only slightly increases. Thus, the Si

428   concentration of the fume stays almost constant. On the other hand, the decreasing Mn fume

429   can be explained by a decrease in the dominant Mn vapor species. This, in turn, can be

430   explained by the decreasing temperature of the system caused by the high heat capacity of

431   water. Increasing MnOH vapor pressure cannot significantly affect the Mn fuming since its

432   partial pressure is comparatively lower (by 6 orders of magnitude) than that of Mn(v).

433   Increasing Si fume and decreasing Mn fume cancel each other out so that the total amount of

434   fume does not noticeably vary with increasing water vapor pressure in the gas phase above

26

435   the SiMn melt. That is, the generated fume only very slightly decreases due to a slight

436   decrease in Mn fume, which is the dominant vapor species.

437   *4.6.2. HCFeMn melt*

438   **HCFeMn melt and gas jet reaction (R1)**

439   In a similar way to the SiMn melt, the oxidation behavior of HCFeMn melt was simulated

440   under different vapor pressures of water in the gas phase at two temperatures, 1823 K and

441   1773 K. The typical HCFeMn composition[8] was used for the calculations. The stable phases

442   from R1 and the gaseous species in 'fume 1' are shown in Figures 13a and b, respectively. As

443   seen, with decreasing temperature, the generated fume as well as the partial pressures of the

444   gaseous species in the fume decrease. With increasing water vapor pressure in the gas phase

445   up to 40 kPa, the amounts of Mn and Fe fume decrease by up to 1 order of magnitude,

446   illustrated in Figure 13b. The amount of the hydroxide gaseous species MnOH increases by

447   about 1 order of magnitude. However, the Zn and SiO amounts of the fume do not noticeably

448   vary with increasing the water vapor pressure in the gas phase. Although the FeMn melt

449   contains a very low concentration of Zn (0.001 wt%), Zn vapor pressure is relatively high (*i.e.*

450   we can assume the surface layer of the melt is almost depleted in Zn). Zinc after Mn is the

451   most dominant vapor species of the fume.

452   In addition, the oxidation behavior of FeMn melt, which has been decarburized at the surface,

453   under dry air and moist air with different vapor pressures of water was simulated in the

454   current work. The results for the decarburized FeMn melt at 1823 K are presented as thick

455   lines in Figure 13. Myklebust et al.[8] observed a large amount of fume from oxidation

456   experiments of HCFeMn in dry air at 1823 K. However, the highest flux values measured

27

457   were above the theoretical limitations of the evaporation flux in vacuo given the alloy bulk

458   composition.[8] This was related to the local decarburization of the melt surface and increased

459   activity of Mn.
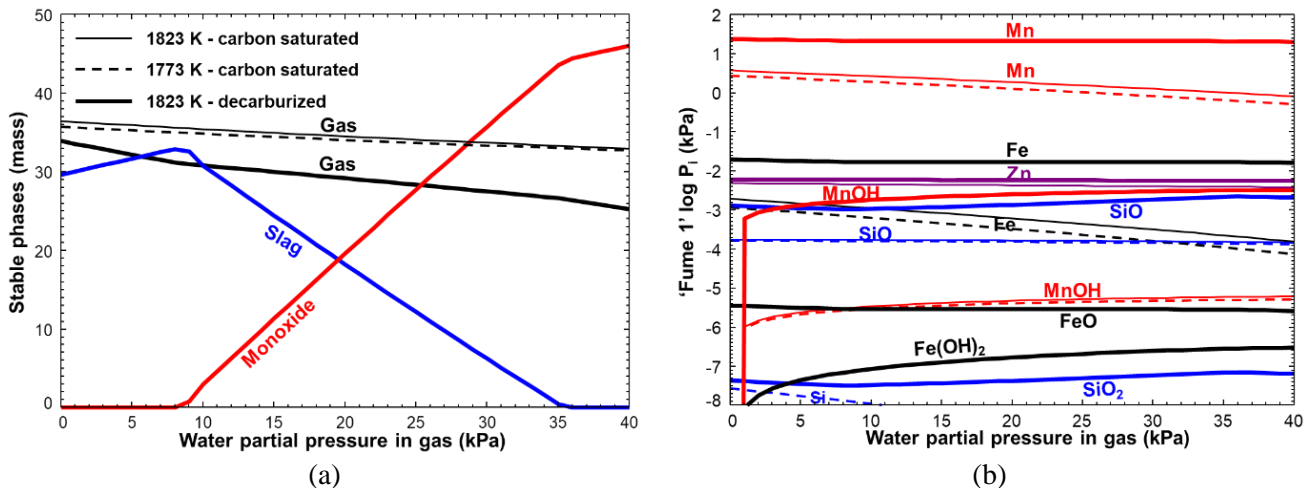
Fig. 13 – Simulated fuming from R1 under different water vapor pressures; (a) reaction products of the gas jet and FeMn melt, and (b) partial pressures of the gaseous species in 'fume1'. The given temperatures are the melt bulk temperature.

460

461   As shown in Figure 13a, as a result of the decarburization of the FeMn melt surface, a lower

462   amount of gas phase is generated (which is related to the absence of CO gaseous component)

463   however, a large amount of the decarburized layer is oxidized to form condensed liquid slag

464   (mainly MnO, 0.3 – 1 wt% SiO_2, and < 1 wt% Mn_2O_3, FeO, Fe_2O_3, P_2O_5, and ZnO) and

465   monoxide phase (mainly MnO plus minor amounts of FeO, Fe_2O_3, and ZnO). This can be

466   explained by the increased partial pressure of oxygen at the decarburized melt surface/gas jet

467   interface (*i.e.* oxygen partial pressure increases from about 10^{-13} kPa for the HCFeMn melt to

468   10^{-9} kPa for the decarburized surface). The transition from the liquid slag to solid monoxide

469   can be explained by the decreased temperature at the melt/gas interface from 2125 K to 2110

470   K at high vapor pressures of water, shifting the local phase equilibrium below the liquidus

471   line in the MnO_x system.

472   As seen in Figure 13b, in the case of the decarburized surface layer of the FeMn melt, the

473   amount of metallic and oxide species such as Mn, Fe, SiO, and MnOH in the fume can be

474   higher than the carbon-saturated melt by 1 to 3 orders of magnitude. According to the

475   calculations, it is only Zn that does not show a significant difference in the presence and

476   absence of carbon. It is also interesting that Mn and Fe vapor pressures only slightly decrease

477   with increasing water vapor pressure in the absence of carbon. On the other hand, the vapor

478   pressure of SiO shows a slight increase with increasing water vapor pressure. These trends

479   are different from the case of carbon saturated melt. This could be because the activity of Mn

480   and Fe is mostly a function of melt composition (*i.e.* the carbon content) and the temperature

481   has a lower impact on the activity of Mn and Fe in the melt, according to the calculations.

482   Moreover, Si and C both compete for oxygen to form $SiO(g)$ and $CO(g)$. Since the formation

483   of $CO(g)$ is thermodynamically more favorable than $SiO(g)$ formation; for the HCFeMn melt,

484   C consumes most of the available oxygen to form $CO(g)$, which partially inhibits the active

485   oxidation of Si to $SiO(g)$ as a result of selective oxidation.

486   The oxidation experiments of HCFeMn melt under moist air (see Figure 3) showed that the

487   generated fume decreases with increasing water vapor pressure in the gas phase which is in

488   agreement with the present calculations for the case of carbon-saturated FeMn melt. As a

489   result, it can be implied that, if the decarburization of the surface layer of FeMn melt had

490   occurred under the moist air atmosphere, the generated amount of fume should have not

491   significantly varied as a function of water vapor pressure according to the present

492   calculations. It is, therefore, possible that the surface decarburization is enhanced under dry

493   air.   This   can   be   explained   by   the   equations $2C+1O_2(g)=2CO(g)$ and

494    $C+1H_2O(v)=CO(g)+H_2(g)$, where 1 mole of O_2 oxidizes 2 moles of carbon while 1 mole of

495   H_2O oxidizes only 1 mole of carbon. That is, a larger extent of decarburization is expected

496   under dry air.

Oxidation reaction across the interface between the melt surface and surrounding gas (R2)

The results of oxidation of 'fume 1' across the interface between the melt surface and surrounding gas (R2) for the HCFeMn melt are depicted in Figure 14. Each condition temperature is imposed by the adiabatic reaction from R1. The fume shows a similar trend to that of SiMn. The difference is the formation of liquid slag at oxygen partial pressures higher than 10^{-2} kPa, which can be explained by the change in the chemistry of the system as a result of oxidation across the interface between melt surface and surrounding gas. The monoxide fume consists of mainly MnO. However, with increasing the oxygen partial pressure across the interface, MnO is partially oxidized to Mn_2O_3 forming the MnO-Mn_2O_3 (MnO_x) liquid slag solution, which has a lower melting point than MnO. The end slag consists of 50 wt% MnO and 50 wt% Mn_2O_3, according to calculations.

Similarly, the oxidation of 'fume 1', generated from the decarburized FeMn melt under dry air at 1823 K, across the interface between melt surface and surrounding gas (R2), was calculated. The results are depicted in Figure 14 as thick solid lines. In comparison to the HCFeMn, a considerably lower amount of gaseous fume and a larger amount of liquid slag fume has been generated. No monoxide fume forms in the case of decarburized FeMn melt, which can be explained by higher oxygen partial pressure at the interface and formation of a considerable amount of Mn_2O_3, having a lower melting temperature in comparison to MnO. However, Figure 14b illustrates that despite lower gas volume due to the absence of CO(g) in the case of a decarburized melt, the partial pressures of Mn and Fe are about 1-2 orders of magnitude higher than those for the HCFeMn melt. The partial pressures of SiO and SiO_2 gaseous species for decarburized FeMn melt show rather complex trends.

1823 K   1773 K
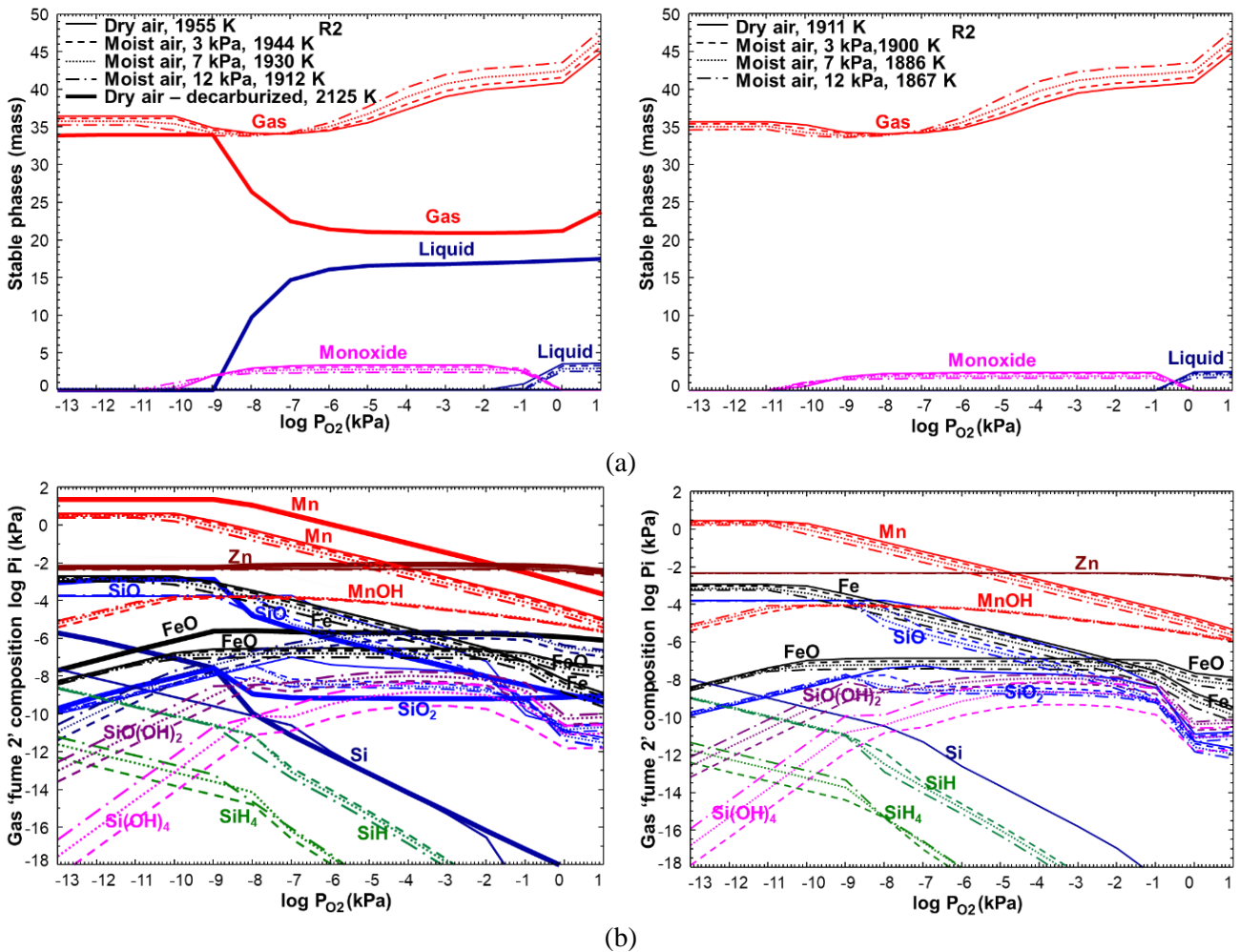
Fig. 14 – Simulated fuming from R2 under different water vapor pressures; (a) reaction products across the interface between melt surface and the surrounding gas, and (b) composition of the gaseous 'fume 2' phase. Thick solid lines represent the calculations for decarburized FeMn melt.

520

Fume condensation and off-gas formation (R3)

522   The 'fume 2' exiting the R2 condenses as a result of the existing temperature gradient. The

523   simulation results are shown in Figure 15 for HCFeMn melt at 1823 K and 1773 K. The main

524   components of the fume are crystalline monoxide and amorphous fume. Others are soot

525   (condensed carbon) and free water. In addition, minor amounts of $Mn_3P_2O_8$, spinel, zincite

526   (mainly ZnO with trace amounts of FeO and Fe_2O_3) form however, they have not been

527   illustrated here. As seen, with increasing water partial pressure in the gas phase, the amount

528 of generated fume decreases. Contrary to the SiMn system where the dominant fume species

529 is amorphous, in the HCFeMn system, crystalline monoxide is the dominant fume constituent.

530 In the case of the SiMn system, the slag is a mixture of MnO, SiO_2, and Mn_2O_3, having a

531 lower melting
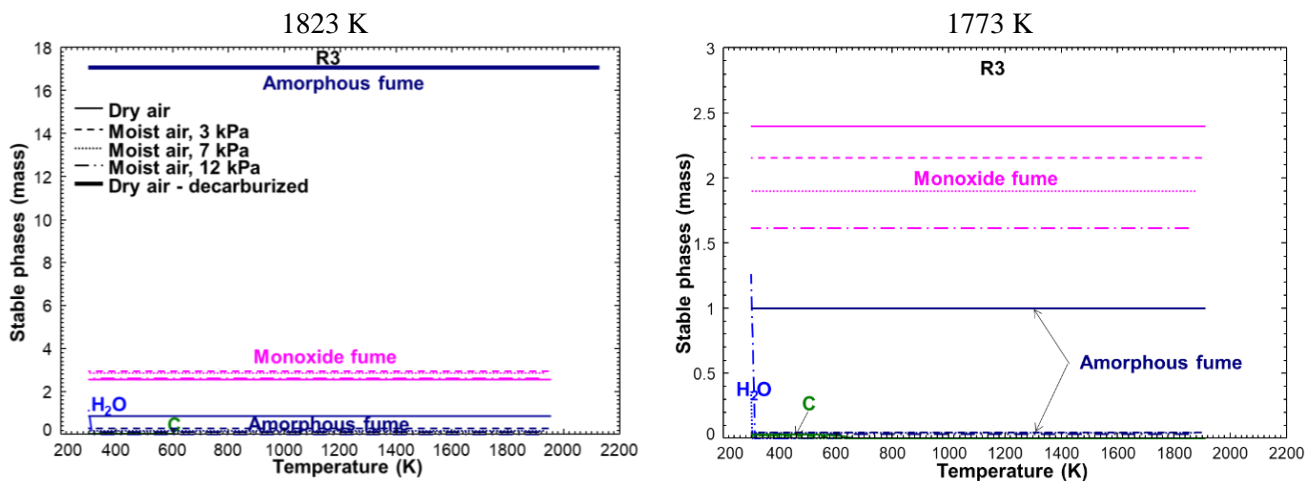
Fig. 15 – Simulated FeMn fuming from R3 under different water vapor pressures; condensed fume

components.

532 temperature in comparison to the slag in the HCFeMn, which mainly consists of MnO.

533 Interestingly, in the case of the decarburized surface layer of FeMn melt, the dominant fume

534 species is amorphous. In this case, the temperature at the melt/gas jet interface increases to

535 about 2125 K while in the case of carbon-saturated FeMn melt, the interface temperature

536 varies between 1955 K and 1912 K for up to 40 kPa water vapor pressure in the gas phase.

537 The higher interfacial temperature shifts the phase equilibrium toward the formation of liquid

538 'fume 2' and subsequently amorphous fume upon condensation. The higher interfacial

539 temperature in the absence of carbon can be explained by the passive oxidation of Mn from

540 the surface layer of the melt. This reaction is extremely exothermic, significantly increasing

541 the interfacial temperature. On the other hand, in the case of carbon saturated melt, although

542 carbon oxidation is also an exothermic reaction, it generates only about 25% of the heat

543   generated from the reaction of 1 mole of Mn and 0.5 moles of oxygen. This can be explained

544   by the enthalpy of the following reactions at 1823 K:

545     $Mn(l)+1/2O_2(g)=MnO(s)$; $\qquad\qquad\qquad\qquad\qquad\qquad\qquad$ ΔH^o (kJ) = -404.282
546   (12)

547     $C+1/2O_2(g)=CO(g)$; $\qquad\qquad\qquad\qquad\qquad\qquad\qquad\qquad$ ΔH^o (kJ) = -117.561

548   (13)
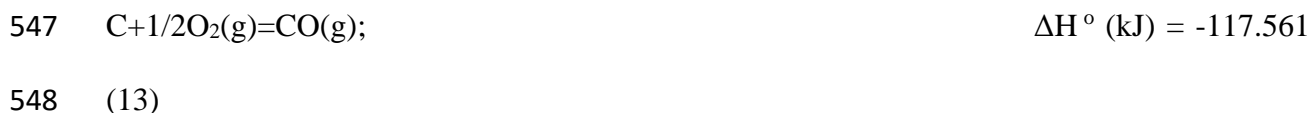
549   **5. Summary of observations and conclusion**

550   The effect of water vapor on the oxidation and fuming of liquid SiMn at 1723 K and 1873 K

551   was experimentally investigated, and compared to the oxidation behavior of HCFeMn melt at

552   1773 K and 1823 K. The chemical reactions of both SiMn and HCFeMn melts with dry air

553   and moist air were also thermochemically modeled under the same experimental variables

554   (composition, temperature, water vapor pressure) using FactSage 8.1 thermochemical

555   software. Equilibrium thermodynamic calculations allowed a better understanding of the

556   mechanisms, underlying the experimental observations. The highlights are summarized

557   below:

558   • In general, the injection of water vapor inhibited the oxidation reaction of Mn, while

559   promoting the oxidation reaction of Si. However, the experimental results showed that

560   there was no significant change in the fuming/oxidation of SiMn melt as a function of

561   water vapor pressure.

562   • The equilibrium thermodynamic calculations for the SiMn system were in agreement

563   with the experimental observations. The vapor pressure of the dominant Si gaseous

564   species in the fume, SiO(g), was almost constant, and only slightly increased with

565   increasing water vapor pressure. On the other hand, the vapor pressure of the

566   dominant Mn gaseous species, Mn(v), only slightly decreased because of decreased

33

567   temperature at the melt surface/gas jet interface under the effect of increasing water

568   vapor pressure. Increasing Si fume and decreasing Mn fume canceled each other out

569   so that the total amount of generated fume did not significantly vary with increasing

570   water vapor pressure.

571 • There was no major morphological difference in the protoparticles of SiMn fume at

572   1873 K between dry and wet air conditions. Analysis of fume samples using TEM

573   revealed that there were no compositional differences as well. The ICP-MS analysis

574   further confirmed that there was no significant difference in the concentrations of

575   main elements in the fume with increasing water partial pressure.

576 • The thermodynamic simulation of the SiMn melt under experimental conditions

577   revealed the formation of amorphous fume under both dry and wet air conditions,

578   which is in accordance with the experimental results. The main components of the

579   amorphous fume were calculated to be MnO (> 70 wt%), SiO_2 (15 – 20 wt%), and

580   Mn_2O_3 (10 wt%).

581 • The experimentally measured fume generated from the HCFeMn melt at both 1773 K

582   and 1823 K decreased with increasing water vapor pressure in the gas phase. The

583   thermodynamic calculations for the carbon saturated FeMn melt agreed with the

584   experimental observations.

585 • According to the thermodynamic calculations, if the decarburization of the surface

586   layer of HCFeMn melt had occurred under moist air, similar to dry air; the generated

587   fume amount should have not noticeably varied as a function of water vapor pressure.

588   This can be explained by the enhanced decarburization of the surface of the FeMn

589   melt under dry air and increased activity of Mn in FeMn melt in the absence of carbon.

590 • Based on the equilibrium thermodynamic simulations, it can be concluded that the Mn

591   activity in the FeMn melt, and subsequently, Mn vapor pressure are mostly a function

592   of melt composition (*i.e.* the carbon concentration), and the temperature has a

593   relatively small effect on the activity of Mn in the melt and its evaporation potential.

594 **Acknowledgments**

598

599 **Conflict of Interest**

600 On behalf of all authors, the corresponding author states that there is no conflict of interest.

References

[1] J. Davourie, L. Westfall, M. Ali, D. McGough: *Neurotoxicol.*, 2017, vol. 58, pp. 180-6.

[2] S. Rencken: Analysis of secondary fume generation and capture during the tapping of high carbon ferromanganese, Department of Chemical Engineering, University of Pretoria, 2013.

[3] M.K. Næss, D.J. Young, J. Zhang, J.E. Olsen, and G. Tranell: *Oxid. Met.*, 2012, vol. 78(5), pp. 363-76.

[4] I. Kero, D. Slizovskiy, B. Wittgens, and G. Tranell: *2015 Sustainable Ind. Process. Summit*, 2015, vol. 3, pp. 135-46.

[5] I. Kero and G. Tranell: *TMS Annu. Meet.*, Nashville, USA: John Wiley & Sons, Inc., Hoboken, New Jersey, 2016, pp. 77-84.

[6] Y. Ma, I. Kero, and G. Tranell: *Oxid. Met.*, 2017, vol. 89(1–2), pp. 211–31.

[7] Y. Ma, E. Moosavi-Khoonsari, I. Kero, and G. Tranell: *Infacon XV: Int. Ferro-Alloys Congr.*, Cape Town, South Africa, 2018.

[8] H.A.H.O. Myklebust, S. Andersson, and G. Tranell: *Oxid. Met.*, 2021, vol. 95(3), pp. 269-90.

[9] P. Cowx, R. Nordhagen, M. Kadkhodabeigi, L. Els, and I. Kero: *Infacon XIV*, Kyiv, Ukraine, 2015.

[10] S.J. Gates, G. Kornelius, I. Kero, and G.M. Tranell: in X. Liu, Z. Liu, K. Brinkman, S. Das, S. Dryepondt, J.W. Fergus, Z. Guo, M. Han, J.A. Hawk, T. Horita, P. Hosemann, J. Li, E. Olivetti, A. Pandey, R.B. Rebak, I. Roy, C. Shang, J. Zhang (Eds.), *Energy Mater. 2017*, Springer International Publishing, Cham, 2017, pp. 73-83.

[11] Y. Ma, B. Jiang, E. Moosavi-Khoonsari, S. Andersson, E. Opila, and G. Tranell: *Ind. Eng. Chem. Research,* 2019, vol. 58, pp. 6785-95.

[12] S.E. Olsen, M. Tangstad, and T. Lindstad, Production of Manganese Ferroalloys, Trondheim, 2007.

[13] D.L. Hildenbrand and K.H. Lau: *J. Chem. Phys.*, 1994, vol. 100(11), pp. 8377-80.

[14] E.J. Opila: *Calphad*, 2016, vol. 55, pp. 32-40.

[15] C.W. Bale, P. Chartrand, S.A. Degterov, G. Eriksson, K. Hack, R. Ben Mahfoud, J. Melançon, A.D. Pelton, and S. Petersen: *Calphad*, 2002, vol. 26(2), pp. 189-228.

[16] https://www.factsage.com/ Accessed December 2021.

[17] L.R. Genskow, W. E. Beimesch, J. P. Hecht, I. C. Kemp, T. Langrish, C. Schwartzbach, and L. Smith, Psychrometry, Evaporative Cooling and Solids Drying, in Perry's Chemical Engineers' Handbook, D. W. Green, Editor. 2008, McGra-HillCompanies Inc.: United States of America. p. 12.5.

[18] M.K. Næss, J.E. Olsen, S. Andersson, and G. Tranell: *Oxid. Met.*, 2014, vol. 82(5-6), pp. 395-413.

643

Table Captions

Table I. Experimental matrix of the current work

Table II. Slag composition measured using EPMA (wt%)

647

648

649

650

651

652

653

654

655

656

657

658

659

660

661

662

663

664

665

666

667

668

669

670

671

672

Figures Captions

Fig. 1 – Flow of equilibrium calculations for simulation of fuming from oxidation process of the melt. Reprinted with permission from reference [11]. Copyright 2019 American Chemical Society.

Fig. 2 – Electron images of slag obtained from SiMn wet air experiments at 1873 K; (a) secondary electron (SE), and (b) backscattered electron (BSE) modes.

Fig. 3 – Mass fluxes of fumes from the FeMn and SiMn melts under different water vapor pressures.

Fig. 4 – Average mass flux of fume from Si melt at 1823 K and SiMn melt at 1873 K as a function of water vapor pressure.

Fig. 5– Typical morphology of SiMn filter fume, generated at (a) 1723 K dry air, (b) 1723 K wet air, (c) 1873 K dry air, and (d) 1873 K wet air conditions.

Fig. 6 – Transition tube fume from SiMn experiments at 1873 K under wet air conditions; (a) TEM bright-field image, (b) relative concentrations of Mn (green color) and Si (red color) in the EEL spectrum image.

Fig. 7 – Filter fume from SiMn experiments at 1873K under wet air conditions; (a) TEM bright-field image, and (b) selected area electron diffraction pattern.

Fig. 8 – Concentrations of Si and Mn in the SiMn fume at 1873 K as a function of water vapor pressure.

Fig. 9 – Particle size distribution of filter fume from SiMn melt at 1873 K under different water vapor pressures, obtained using (a) LD and (b) SEM image counting.

694   Fig. 10 – Simulated fuming from R1 under different water vapor pressures; (a) reaction

695   products of the gas jet and SiMn melt, and (b) partial pressures of the gaseous species in

696   'fume1'.

697   Fig. 11 – Simulated fuming from R2 under different water vapor pressures; (a) reaction

698   products across the interface between SiMn melt surface and the surrounding gas, (b)

699   composition of the gaseous 'fume 2', and (c) composition of liquid 'fume 2'. The labeled

700   temperatures come from the adiabatic reaction in R1.

701   Fig. 12 – Simulated SiMn fuming from R3 under different water vapor pressures; (a – c)

702   condensed fume components.

703   Fig. 13 – Simulated fuming from R1 under different water vapor pressures; (a) reaction

704   products of the gas jet and FeMn melt, and (b) partial pressures of the gaseous species in

705   'fume1'. The given temperatures are the melt bulk temperature.

706   Fig. 14 – Simulated fuming from R2 under different water vapor pressures; (a) reaction

707   products across the interface between melt surface and the surrounding gas, and (b)

708   composition of the gaseous 'fume 2' phase. Thick solid lines represent the calculations for

709   decarburized FeMn melt.

710   Fig. 15 – Simulated FeMn fuming from R3 under different water vapor pressures; condensed

711   fume components.